

Article

Room-Temperature Liquid-Metal Coated Zn Electrode for Long Life Cycle Aqueous Rechargeable Zn-Ion Batteries

Weldejewergis Gebrewahid Kidanu ^{1,2}, Hyewon Yang ¹, Saemin Park ¹, Jaehyun Hur ^{1,*} and Il Tae Kim ^{1,*}

¹ Department of Chemical and Biological Engineering, Gachon University, Seongnam-si 13120, Gyeonggi-do, Korea

² Department of Chemical Engineering, Ethiopian Institute of Technology-Mekelle (EIT-M), Mekelle University, Mekelle 231, Tigray, Ethiopia

* Correspondence: jhhur@gachon.ac.kr (J.H.); itkim@gachon.ac.kr (I.T.K.); Tel.: +82-31-750-5593 (J.H.); +82-31-750-8835 (I.T.K.); Fax: +82-31-750-5776 (J.H.); +82-31-750-5363 (I.T.K.)

Abstract: Aqueous rechargeable zinc-ion batteries (ARZIBs) are potential candidates for grid-scale energy storage applications. In addition to its reversible chemistry in aqueous electrolytes, Zn metal is stable in water and air. However, there are critical challenges, such as non-uniform plating, hydrogen evolution, corrosion, and the formation of a passivation layer, which must be addressed before practical applications. In this study, the surface of Zn metal was coated with room-temperature bulk liquid-metal and liquid-metal nanoparticles to facilitate the uniform plating of Zn-ions during cycling. A simple probe ultrasonication method was used to prepare the liquid-metal nanoparticles, and a nanoparticle suspension film was formed through spin coating. At an areal capacity and current density of 0.5 mAh cm^{-2} and 0.5 mA cm^{-2} , respectively, symmetric cells composed of bare Zn metal electrodes were prone to short-circuiting after $\sim 45 \text{ h}$ of deposition/stripping cycles. However, under the same operating conditions, symmetric cells employing the room-temperature liquid-metal-coated electrodes operated stably for more than 500 h. Compared to the symmetric cell with bare Zn, the symmetric cell with the bulk liquid-metal coated electrode exhibited a significant reduction in the initial nucleation barrier, with respective values of 113.2 and 10.1 mV. Electrochemical characterization of practical full cells also showed significant improvements in the capacity and cycling performance derived from the room-temperature liquid-metal coating.

Keywords: aqueous zinc ion battery; liquid-metal coating; liquid-metal nanoparticle coating; surface engineering



Citation: Kidanu, W.G.; Yang, H.; Park, S.; Hur, J.; Kim, I.T.

Room-Temperature Liquid-Metal Coated Zn Electrode for Long Life Cycle Aqueous Rechargeable Zn-Ion Batteries. *Batteries* **2022**, *8*, 208.

<https://doi.org/10.3390/batteries8110208>

Academic Editors: Guojin Liang and Funian Mo

Received: 8 October 2022

Accepted: 28 October 2022

Published: 2 November 2022

Publisher's Note: MDPI stays neutral with regard to jurisdictional claims in published maps and institutional affiliations.



Copyright: © 2022 by the authors. Licensee MDPI, Basel, Switzerland. This article is an open access article distributed under the terms and conditions of the Creative Commons Attribution (CC BY) license (<https://creativecommons.org/licenses/by/4.0/>).

1. Introduction

Compared to fire-prone commercial lithium-ion batteries (LIBs), aqueous rechargeable Zn-ion batteries (ARZIBs) are inherently safer, environmentally compatible [1–3], ~ 300 times more abundant [3,4], and cost-effective (i.e., they can be safely handled in ambient environments) [3,5,6]. The enhanced rate of performance of aqueous batteries is believed to be derived from their high ion transport rate at the electrode–electrolyte interface [7–9]. ARZIBs are less sensitive to air and humidity [10,11]. More interestingly, the Zn anode has a high electronic conductivity, high capacity (820 mAh g^{-1} , ~ 2.2 times greater compared to that of the commercial graphite electrode ($820 \text{ vs. } 374 \text{ mAh g}^{-1}$)), low redox potential (-0.76 V vs. standard hydrogen electrode), reasonably low polarizability, and can be manufactured via a simple process compared to other anode materials such as Mg and Al [12–14]. Thus far, ARZIB research has mainly focused on cathode materials, whereas the problem on the anode side has been addressed by utilizing excess (by mass) Zn. Nonetheless, recently, the anode has garnered renewed attention as the Zn metal electrodes in ARZIBs have a salient effect on the overall electrochemical performance. However, conventional Zn-metal-electrode-based ARZIBs suffer from poor reversibility, low coulombic efficiency (CE), catastrophic dendrite growth (due to non-homogeneous

plating), and severe self-corrosion [12,15,16]. Research to optimize the operation of Zn metal electrodes in mild aqueous electrolytes to overcome these barriers is still in the development stage [12,17,18].

The current challenges hindering the industrialization of ARZIBs can be categorized as dendrite formation during repeated cycling, sustained electrolyte consumption leading to self-discharge, and the formation of side products (such as a ZnO passivation layer) [12,19]. Several strategies, such as modification of the electrode–electrolyte interface, electrolyte engineering [20,21], surface coating [22–26], design of porous structures, utilizing 3D material supports [27–31], and self-healing [32], have been suggested as means of preventing dendrite formation and minimizing side reactions. The formation of Zn dendrites is not easily suppressed due to the ‘tip effect’, where once nucleation is initiated, the incoming ions, by nature, prefer to adhere to the previously formed crystals due to the difference in surface energy [7]. Hence, the ultimate surface morphology of the Zn plating depends on the initial nucleation and growth conditions [33]. Therefore, developing methods to enable uniform initial Zn ion deposition can potentially alleviate or prevent dendrite formation. Surface coating is one of the most crucial strategies for improving the interfacial stability and cyclability of Zn metal electrodes [12], as the solid electrolyte interface (SEI) in Zn is not continuous, as in the case of alkali metal electrodes. Surface coating with thin films helps suppress surface reactions and dissolution of the cathode materials. For example, Alshareef and his colleagues used hafnium oxide film coated with $Zn_3V_2O_7(OH)_2 \cdot 2H_2O$ as a synthetic SEI to prevent vanadium dissolution [24].

Herein, the surface of a Zn anode is coated with room-temperature GaIn eutectic (EGaIn) bulk liquid-metal (BLM) and EGaIn liquid-metal nanoparticles (LMNPs). Compared with their solid-metal-electrode counterparts, the fluidic and flexible/deformable nature of liquid-metals and metal alloys lead to inherently dendrite-free and/or self-healable properties. However, room-temperature liquid-metal and liquid-metal alloys do not require energy input to maintain their liquid state, as is required in the case of high-temperature molten electrode materials; therefore, the former may afford higher energy conversion efficiency, less possibility of corrosion as a result of high temperature, as well as increased safety compared to that of high-temperature liquid-metal batteries [34]. Furthermore, gallium-based room-temperature liquid-metal alloys (such as GaInSn, GaIn, and GaSn) have low toxicity and low vapor pressure (despite the low melting point of 29.8 °C, Ga has a high boiling point of 2400 °C and zero vapor pressure at room temperature) [35], good chemical stability, excellent fluidity, and high electrical and thermal conductivities [36]. The low toxicity, low vapor pressure, and good chemical stability of Ga-based liquid metals allow safer handling without the risk of evaporation, even under high vacuum conditions [35,37]. Hence, herein, a gallium indium eutectic (EGaIn) room-temperature liquid-metal is used as a coating material for Zn metal anodes in aqueous Zn ion batteries.

2. Materials and Methods

2.1. Reagents and Materials

EGaIn (99.99% metal basis, Ga: In ratio of 74.5:24.5, wt%), Zn metal foil (99.98% metal basis, 0.25 mm thick), and sodium dodecyl sulfate (SDS) surfactant were purchased from Alfa Aesar (Ward Hill, MA, USA). The EGaIn liquid metal nanoparticles (LMNPs) were prepared in this study.

2.2. Coating and Preparation of EGaIn Liquid-Metal Nanoparticles (LMNPs)

For the bulk liquid-metal coating, a simple brush coating method was used to coat the surface of the Zn foil with EGaIn. For the liquid-metal nanoparticle (LMNP) coating, the nanoparticles were ultrasonicated using a Sonics Vibra-cell ultrasonic liquid processor (VCX750). In detail, 50 mg of EGaIn was added to 1 mL of N-methyl-2-pyrrolidone (NMP), and 1 mg of SDS surfactant was used to prevent possible agglomeration of the LMNPs. The pulse was on and off, respectively, for 40 s and 55 s and was repeated for 2 h. The ultrasonication condition is as described in our previous study [38]. The thickness of the

bulk liquid metal and liquid metal nanoparticle coating was measured by a high-accuracy micrometer scale caliper (Mitutoyo, 0.001~0.25 mm, Japan). The bare and coated Zn metal anodes were then punched into a coin size, 12.5 mm in diameter. Before preparing the bare and coated Zn coins, the Zn foil was cleaned via ultrasonication with water and ethanol. The mass of the bare Zn electrode with a diameter of 12.5 mm was measured to be ~220 mg, while the average thickness of the bulk liquid metal coating and liquid metal nanoparticle coating layers was measured to be 1.5 μm and 1.0 μm , respectively.

2.3. Materials Characterization

The surface morphology of the Zn electrode before and after coating was analyzed using optical microscopy (Keyence Corporation, Osaka, Japan). Scanning electron microscopy (SEM) measurements were performed to study the surface morphology. Electron diffraction spectroscopy (SEM/EDS) was deployed to investigate the elemental composition of the electrodes.

2.4. Preparation of Cathode Material and Electrochemical Measurements

Commercial V₂O₅ powder (99.6%, Alfa Aesar, Ward Hill, MA, USA) was ball-milled with carbon black (80:20, wt%) using a Pulverisette 5 planetary mill (Fritsch GmbH, Idar-Obersten, Germany). Milling was performed for 1 h at 300 rpm with a 30 min rest, and the process was repeated three times. The ball-milled product was labeled V₂O₅@C and mixed with carbon black and polyvinylidene fluoride (65:25:10, wt%) to prepare a slurry. NMP was used as a solvent to homogenize the slurry, which was finally cast on a titanium current collector (0.032 mm thick, 99.7% annealed, Alfa Aesar, Ward Hill, MA, USA), followed by drying overnight at 70 °C under vacuum. Thereafter, symmetric and full CR2032 type coin cells were assembled in an ambient atmosphere with a glass fiber separator (Merck Millipore, Cork, Ireland) and a commercial 2 M ZnSO₄ electrolyte (Sigma Aldrich, Steinheim, Germany). The symmetric cells (the electrochemical cells utilizing the same bare or coated Zn electrode as both anode and cathode) were operated at an areal capacity and current density of 0.5 mAh cm^{-2} and 0.5 mA cm^{-2} , respectively. Galvanostatic charge-discharge (GCD) cycling studies were performed using a constant current (CC) mode WBCS3000 automatic battery cycling system (WonATech, Seoul, South Korea; at the Smart Materials Research Center for IoT at Gachon University). Cyclic voltammetry (CV) and electrochemical impedance spectroscopy (EIS) analyses were conducted using a ZIVE MP1 electrochemical system (WonATech, Seoul, South Korea). For the CV studies, a scan rate of 50 $\mu\text{V s}^{-1}$ was applied, and for the EIS measurements of the bare Zn/Zn and EGaIn LM@Zn/EGaIn LM@Zn symmetric cells before and after cycling, a perturbation potential of 5×10^{-3} V was used between a frequency region of 10⁵ Hz and 10⁻³ Hz.

3. Results and Discussion

A schematic of the crystal growth in the bare Zn and liquid-metal-coated Zn is presented in Figure 1a,b. As shown in the schematic, the Zn deposition/stripping process in the bare electrodes (Zn anode) leads to the evolution of sharp dendrites (Figure 1a), which can later disrupt the separator and cause short-circuiting and cell failure [39]. In contrast, in the bulk liquid metal-coated (Zn@BLM) and liquid-metal nanoparticle-coated (Zn@LMNP) electrodes, the plating/stripping process led to evenly distributed crystal growth (Figure 1b). Figure 1c–e show the SEM images of the bare Zn anode, Zn@BLM, and Zn@LMNP electrodes, respectively. The SEM images of Zn@BLM and Zn@LMNP in Figure 1d,e show that the room-temperature liquid-metal was distributed all over the electrode surfaces. More interestingly, as illustrated in the low-magnification SEM images of the Zn@BLM and Zn@LMNP electrodes, the distribution of the liquid-metal particles was better in the bulk liquid-metal-coated electrode. This may be due to the greater tendency of LMNPs to attract each other as a result of the high surface tension. SEM/EDS elemental maps of the electrodes are presented in Figure 2. The average thickness of

the bulk liquid metal and liquid metal nanoparticle layer was estimated to be 1 μm and 1.5 μm , respectively.

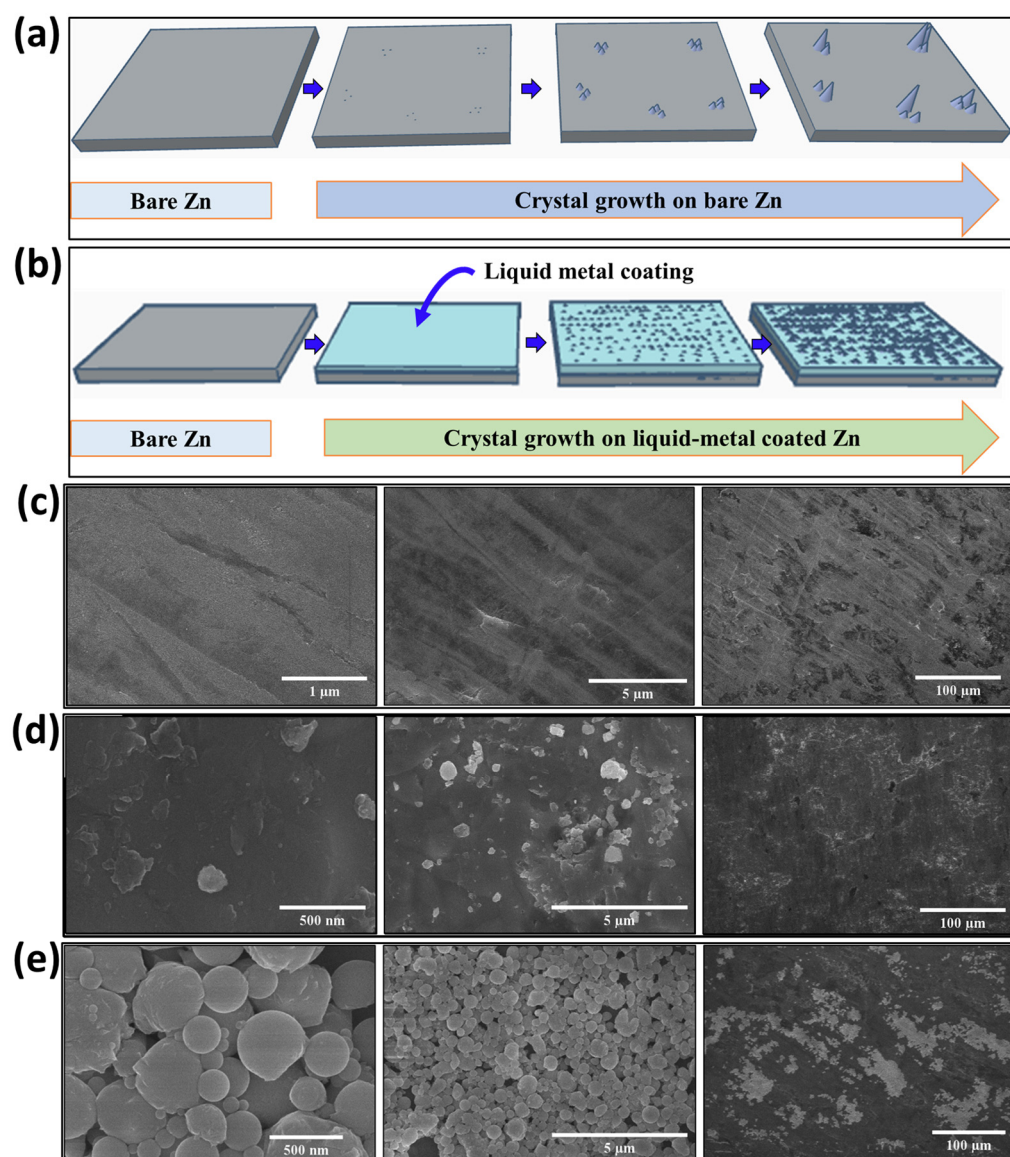


Figure 1. Schematic of Zn^{2+} ion deposition/stripping in (a) bare Zn anode and (b) in room-temperature bulk liquid-metal-coated Zn@BLM electrodes; SEM images of (c) bare Zn anode; (d) Zn@BLM and (e) Zn@LMNP electrodes.

To examine the gap between the charge and discharge voltages, voltage hysteresis, and polarization, various coin-cell-type symmetric cells were investigated at different cycling times. The voltage–capacity profiles of the bare $\text{Zn} \parallel \text{Zn}$, Zn@BLM \parallel Zn@BLM, and Zn@LMNP \parallel Zn@LMNP symmetric cells at the 1st, 2nd, and 10th cycles are shown in Figure 3a–c. At an areal capacity of 0.5 mAh cm^{-2} and a current density of 0.5 mA cm^{-2} , the voltage hysteresis between the first deposition/stripping process of the symmetric bare $\text{Zn} \parallel \text{Zn}$, Zn@BLM \parallel Zn@BLM, and Zn@LMNP \parallel Zn@LMNP cells was estimated to be 151, 8, and 65 mV, respectively (Figure 3d–f). The voltage hysteresis of the Zn@BLM \parallel Zn@BLM symmetric cell was 19 times lower than that of the bare $\text{Zn} \parallel \text{Zn}$ symmetric cell (151 mV vs. 8 mV) and eight times lower than that of the Zn@LMNP \parallel Zn@LMNP (65 mV vs. 8 mV) symmetric cells. The voltage hysteresis is the gap between the charge and discharge voltages of the symmetric cells; therefore, the lowest voltage hysteresis in the Zn@BLM \parallel Zn@BLM symmetric cell indicates the highest coulombic (or energy) efficiency

of the system [40]. The voltage hysteresis is caused by measuring the resistance of the surface to the Zn^{2+} deposition or stripping reactions. It is significantly affected by the presence of uniformly or randomly spotted reaction sites. As described in a previous study [30], heterogeneous seeds can effectively assist cation deposition and spatial control of initial nucleation. Hence, the bulk liquid metal coated, and liquid metal nanoparticle coated electrodes, which have an evenly distributed morphology of liquid metals, could act as favorable nucleation sites for the Zn^{2+} ion distributions. The significant improvement in the voltage hysteresis was further explored by studying the cycling life-span and stability of the symmetric cells.

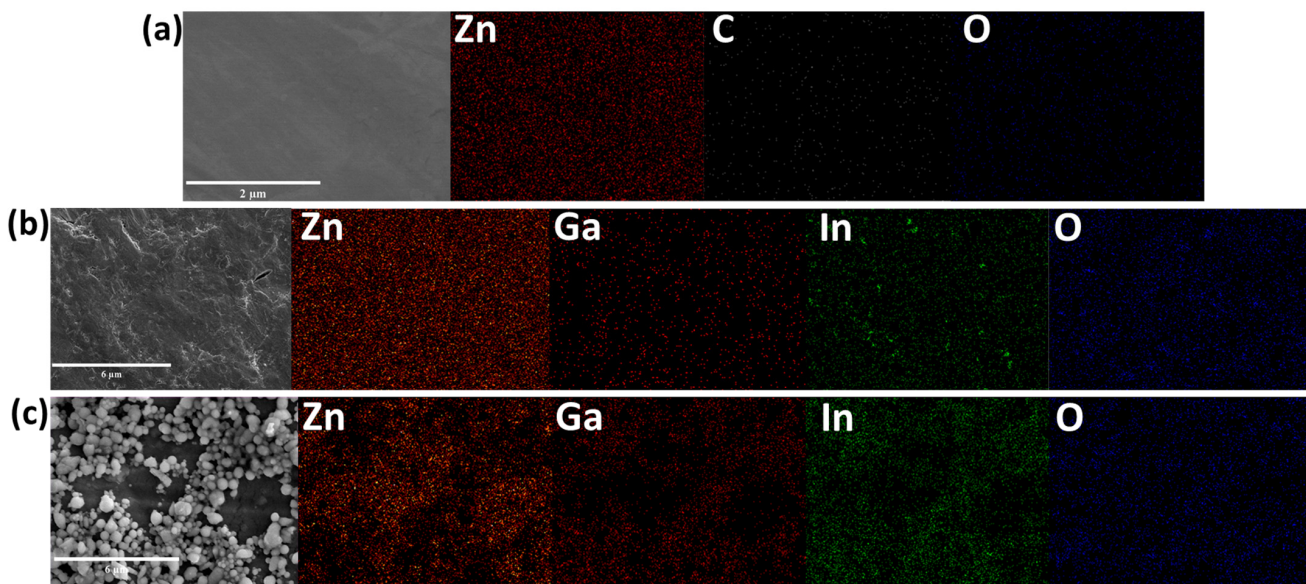


Figure 2. SEM/EDS elemental mapping images of (a) bare Zn anode, (b) Zn@BLM, and (c) Zn@LMNP electrodes.

The charge–discharge profiles at different times and the corresponding initial nucleation overpotentials of the three symmetric cells are exhibited in Figure 4. In the symmetric cell with bare Zn electrodes, the deposition/stripping process was unstable and irregular, and the polarization voltage was much higher (~40 mV), resulting in short-circuiting in less than 20 h of cycling, as depicted in Figure 4a,b. This is in agreement with the random nucleation process on the bare Zn electrode, as schematically displayed in Figure 1a. Fluctuations in the initial overpotentials of the bare Zn symmetric cells can be caused by the uneven deposition of Zn^{2+} ions on the rough morphology of the bare Zn electrode [41–43]. Furthermore, the charge/discharge properties in Figure 4b,c indicate more facile and smoother Zn plating and stripping in the Zn@BLM symmetric cells; specifically, the initial overpotential barrier for the bare Zn, Zn@BLM, and Zn@LMNP symmetric cells were 113.2, 62.9, and 10.1 mV, respectively (Figure 4d–f). This striking difference shows that the initial nucleation barrier on the bare Zn electrode is eleven times higher (113.2 mV vs. 10.1 mV, more than 1000% higher), and two times (113.2 mV vs. 62.9 mV) higher than the nucleation overpotential on the Zn@BLM and Zn@LMNP electrodes, respectively. Such a low and stable initial nucleation overpotential is a good indicator of facile ion transfer at the electrode/electrolyte interface [41,44,45]. It is noted that the LMNP coating layer could act as nanoseeds to guide the deposition of the Zn^{2+} ions, thereby significantly decreasing the nucleation overpotential. In a previous report by Yang et al. (2017), Ag nanoparticles exhibited similar effects during the deposition of Li-ions [30]. Hence, the short-circuiting in the bare Zn-symmetric cells is attributed to the high nucleation barrier. The long-term voltage–time profiles are shown in Figure 4g. The outstanding cycling stability of the Zn@BLM || Zn@BLM symmetric cell indicates that the proposed interfacial engineering had a significant positive impact on the electrodes. The short-circuiting in

the bare Zn/Zn symmetric cell is mainly related to the uneven plating and stripping of Zn^{2+} ions on the bare Zn electrode, which led to dendrite growth and ultimately pierced the separator. From the evaluation of the symmetric cells, it is notable that although the voltage polarization was smaller and the stability in the initial cycles was much better than that of the cell with bare Zn, the symmetric cell with the Zn@LMNP electrodes was prone to short-circuiting after ~45 h of deposition/stripping cycles. In a sharp contrast, the symmetric cell with the Zn@BLM electrodes not only operated stably for more than 500 h under the same experimental conditions (areal capacity of 0.5 mAh cm^{-2} and current density of 0.5 mA cm^{-2}) but also exhibited the lowest polarization voltage and lowest voltage hysteresis. Therefore, to further understand the differences in the performance of the Zn@BLM and Zn@LMNP electrodes, the initial nucleation overpotential and long-term cycling performance of the symmetric cells were thoroughly examined. As depicted in Figure 4c–f, the initial nucleation overpotential of the bare and coated Zn electrodes, and the constant current charge–discharge behavior upon cycling of the bare Zn || Zn, Zn@BLM, and Zn@LMNP symmetric cells were investigated. The coulombic efficiencies of the cells were also plotted. As presented in Figure S1, the average coulombic efficiencies of the bare Zn || Zn, Zn@BLM || Zn@BLM, and the Zn@LMNP symmetric cells were 99.16%, 99.1%, and 99.22%, respectively. EIS was used to study the resistance and rate of charge transfer at the electrode/electrolyte interface. The Nyquist plots from the EIS data after the long-term cycling tests of the symmetric cells are shown in Figure 4h. From the EIS measurements, the charge transfer resistance of the bare Zn || Zn, Zn@BLM || Zn@BLM, and Zn@LMNP || Zn@LMNP symmetric cells after the long-term cycling test was estimated to be 4500, 23, and 250 Ω , respectively (Figure 4h). The charge transfer resistance is basically defined as the resistance of the electrode surface during deposition/stripping reactions. Hence, the remarkably low charge-transfer resistance of the Zn@BLM || Zn@BLM symmetric cell indicates that charge deposition and stripping in the Zn@BLM electrodes are much easier than in the case of the bare Zn electrodes, which is another reason for the stable long-term cyclability of the cell.

After the symmetric cell studies, the electrodes were subjected to postmortem analysis using optical microscopy and scanning electron microscopy (Figure 5). Figure 5a shows an optical image of the smooth surface of the fresh bare Zn electrode, while Figure 5b–d present the ex situ optical images of the bare Zn, Zn@BLM, and Zn@LMNP electrodes after long-term symmetric cell studies, respectively. Supporting the early failure of the symmetric cell with the bare Zn electrodes, large dendrites were observed in the bare Zn metal anode (Figure 5b). As shown in Figure 5c, the distribution of the deposited mass in the Zn@BLM anodes was relatively even, which explains the long-term stability of the Zn@BLM || Zn@BLM symmetric cell. The optical image of the Zn@LMNP electrode also exhibited more uniform Zn^{2+} deposition than in the case of the bare Zn electrode; however, there was a great tendency for agglomeration in the former (Figure 5d).

Ex situ SEM images of the anode-side electrodes of the symmetric cells are presented in Figure 5e–g. In line with the above discussion, the ex situ SEM image in Figure 5e shows a large mass detached from the surface of the bare Zn electrode. This implies that Zn^{2+} ion deposition was concentrated in small high-electric-field spots, leading to dendrite formation. From the ex situ SEM images in Figure 5f,g, it can be further confirmed that the Zn^{2+} ion distribution was relatively uniform in the Zn@BLM electrodes (Figure 5g). The strong hips (the white areas in the low-resolution image in Figure 5g) in Zn@LMNP explain the early failure of the Zn@LMNP || Zn@LMNP symmetric cell. As described below, the same conclusions were obtained from the full-cell studies.

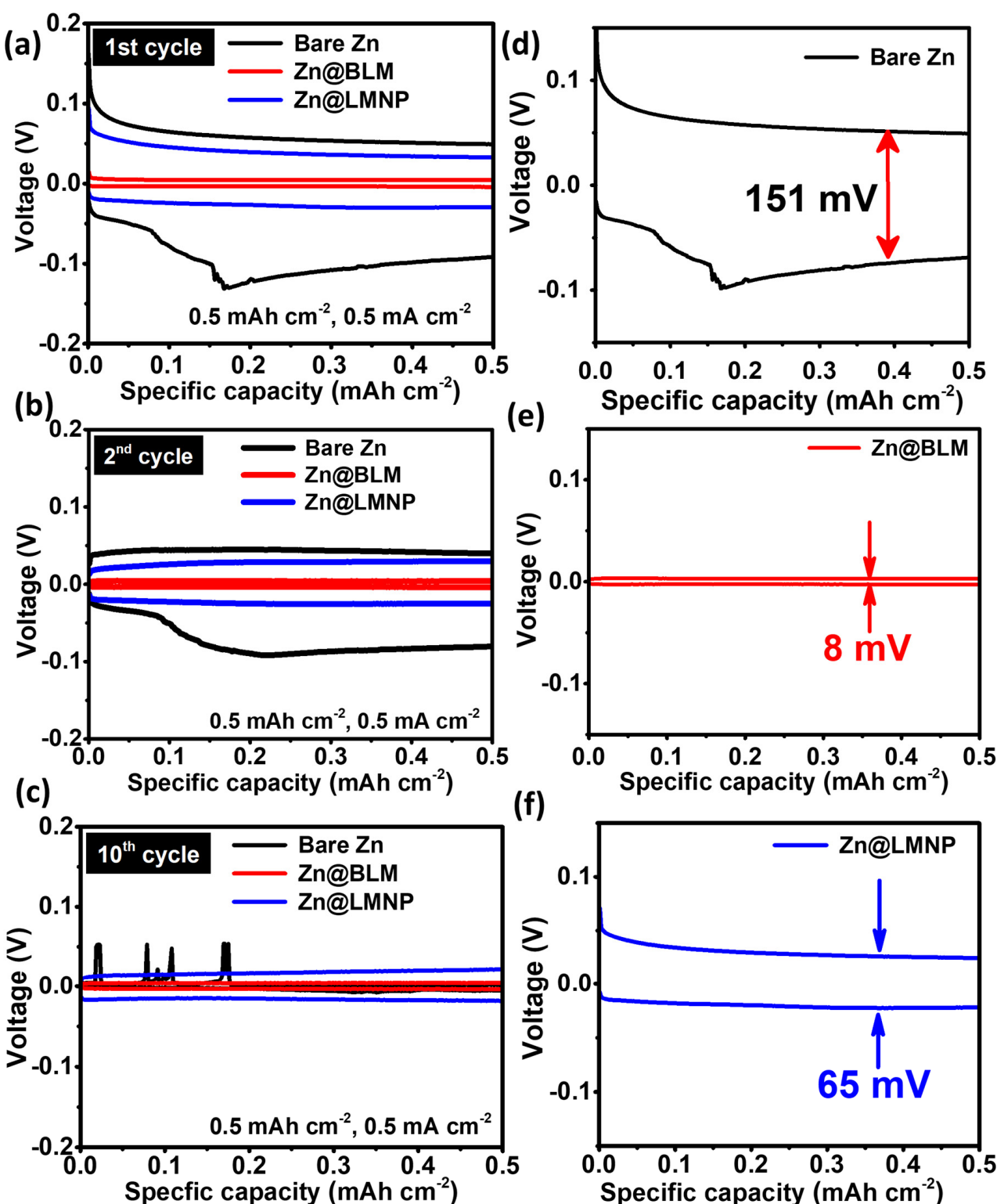


Figure 3. Voltage–specific capacity curves of bare Zn, Zn@BLM, and Zn@LMNP symmetric cells at the typical (a) first, (b) second, and (c) tenth cycles at a capacity of 0.5 mAh cm^{-2} and current density of 0.5 mA cm^{-2} . Voltage hysteresis (the gap between reversible and irreversible capacity) in the first cycle for the (d) bare Zn, (e) Zn@BLM, and (f) Zn@LMNP electrodes.

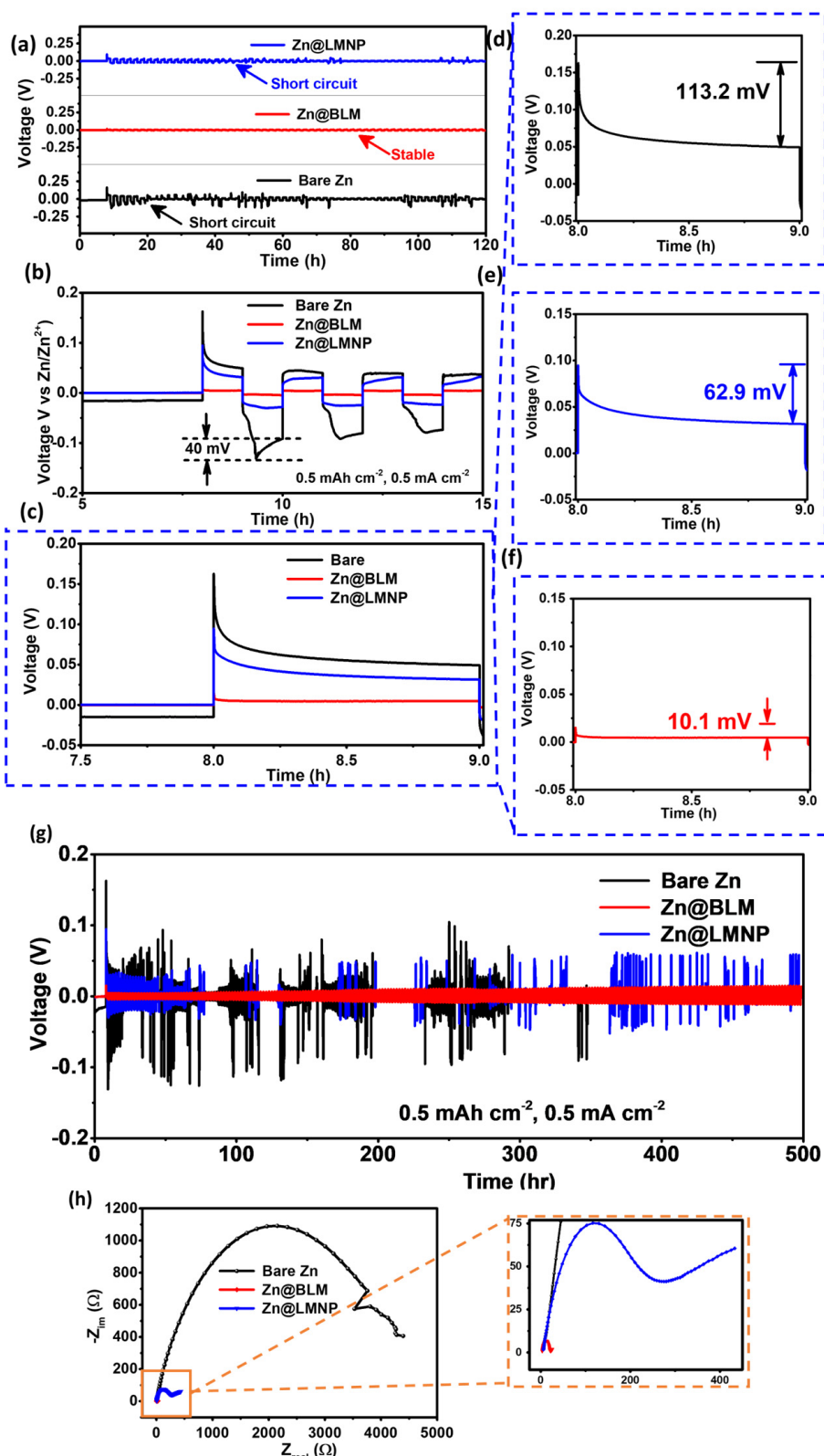


Figure 4. (a–c) Charge–discharge voltage behaviors, (d–f) corresponding initial nucleation overpotentials, and (g) long-term Zn depositing/stripping test of bare Zn || Zn, Zn@BLM || Zn@BLM, and Zn@LMNP || Zn@LMNP symmetric cells at 0.5 mA cm^{-2} and 0.5 mAh cm^{-2} . (h) EIS profiles of the symmetric cells after long-term cycling.

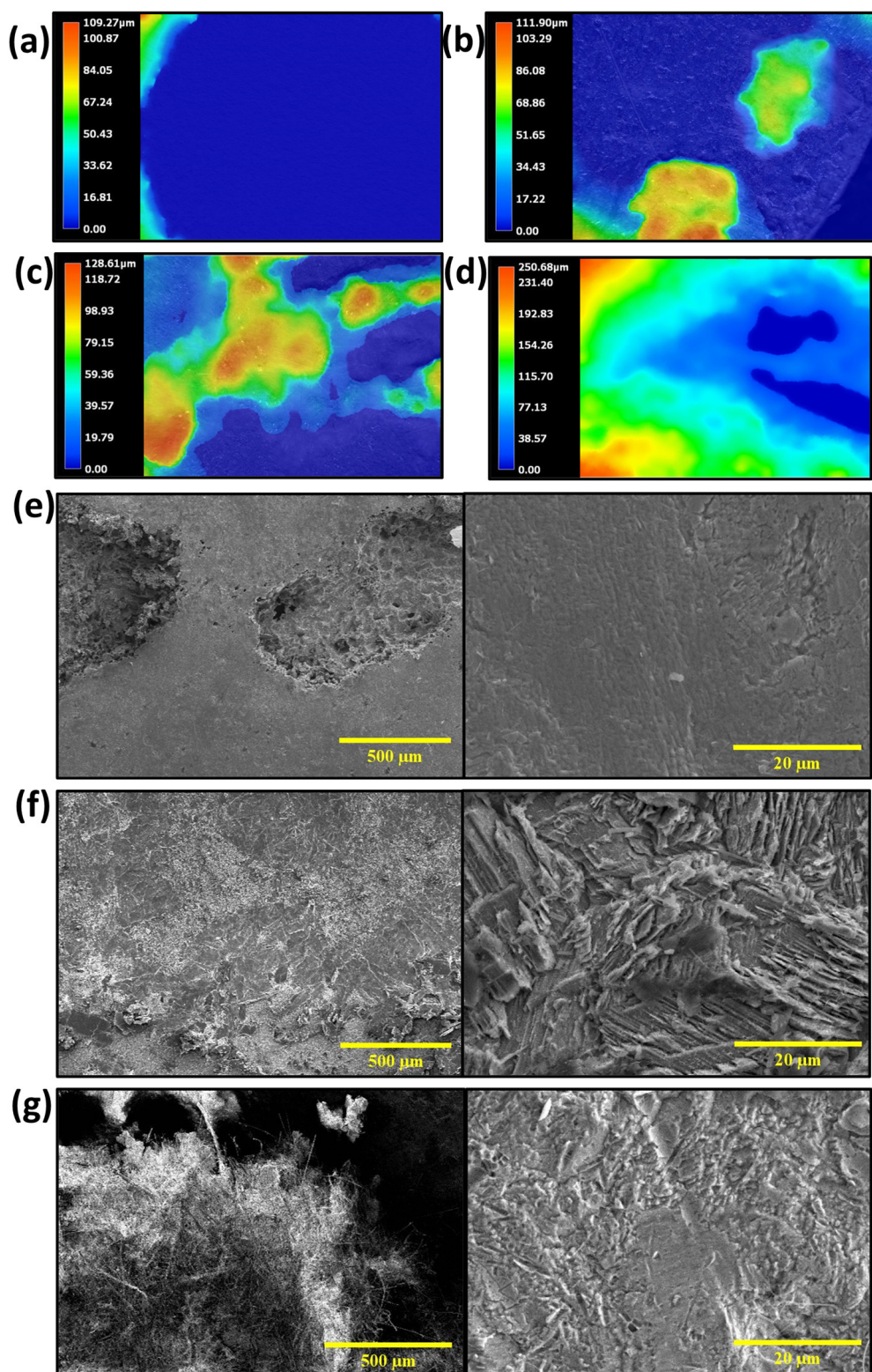


Figure 5. Optical microscope images and ex situ SEM images of electrodes from the various symmetric cells. Optical microscope images of (a) fresh Zn, (b) cycled bare Zn, (c) cycled Zn@BLM, and (d) cycled Zn@LMNP. SEM images of the anode-side electrode of the (e) bare Zn || Zn cell, (f) Zn@BLM || Zn@BLM cell, and (g) Zn@LMNP || Zn@LMNP cell after long-term cycling of the symmetric cells in Figure 4g.

To further study the effectiveness of the room-temperature liquid-metal coating, the electrochemical performance of full cells with the different anodes was investigated, as presented in Figure 6. In principle, the nucleation of a new solid phase requires overcoming the free energy barrier [33,46]. The unique features of the initial potential profiles (Figure 6) can be attributed to the nucleation barrier. As illustrated in Figure 6a–c and as highlighted in Figure 6d, the room-temperature liquid-metal coating decreased the nucleation barrier from ~0.06 V for the bare Zn metal electrode to ~0.04 V for the Zn@BLM electrode. Remarkably, the nucleation barrier for the Zn@LMNP electrode was nearly zero. The coating of the Zn metal electrode with the Zn-reactive EGaIn room-temperature liquid-metal reduced the nucleation barrier [47]. A similar negligible nucleation overpotential was observed when nucleation seeds such as Au, Ag, Zn, or Mg were introduced into lithium [33,48]. It is also well known that the nucleation barrier determines the nucleation number density and nuclei size [33,49,50]. This can be explained in terms of the surface resistance of the bare and coated Zn electrodes. As shown in Figure 6d, the rebound potential decreased for the Zn@LMNP electrode compared to that of the bare Zn electrode, corresponding to a decrease in the initial internal resistance [51]. This will have a significant effect on the ultimate morphology of the electrode after several galvanostatic charge–discharge cycles; hence, the highest capacities obtained with the Zn@LMNP electrode could be attributed to the lowest nucleation barrier owing to the reasonably distributed nucleation sites. The short- and long-term cycling performance of the full cells was also evaluated. As deduced from Figure 6e, the room-temperature liquid-metal coating, in general, enhanced the discharge capacity of the full cell. The initial discharge capacities (and coulombic efficiencies) of the full cells with bare Zn, Zn@BLM, and Zn@LMNP were 120 (35.5%), 213.4 (50.4%), and 236.4 mAh g^{−1} (19%), respectively. After nearly 20 stabilization cycles, the full cells delivered maximum discharge capacities (and coulombic efficiencies) of 278 (98%), 417 (90%), and 538 mAh g^{−1} (92%) for the cells with the bare Zn, Zn@BLM, and Zn@LMNP anodes, respectively (Figure 6e,f). The results of the long-term cyclability and coulombic efficiency tests are presented in Figure 6g,h, respectively. Although the full cell with the Zn@LMNP anode displayed the highest discharge capacity, this cell failed after ~200 cycles. This failure is attributed to aggregation of the distributed LMNPs during cycling, which could lead to dendrite growth or mass detachment from the electrode surface [52]. The failure can also be attributed to continued electrolyte consumption caused by the high surface area of the nanoparticles, which might lead to a short cycle life [53]. Gallium and gallium alloys have high surface energies; for instance, gallium has a surface energy of ~700 mN m^{−1}, and EGaIn has a surface energy of ~500 mN m^{−1} [54]. Overall, the liquid-metal coating enhanced the cyclability and capacity of the aqueous Zn-ion batteries by guiding a relatively even distribution of the ions during the deposition and stripping processes.

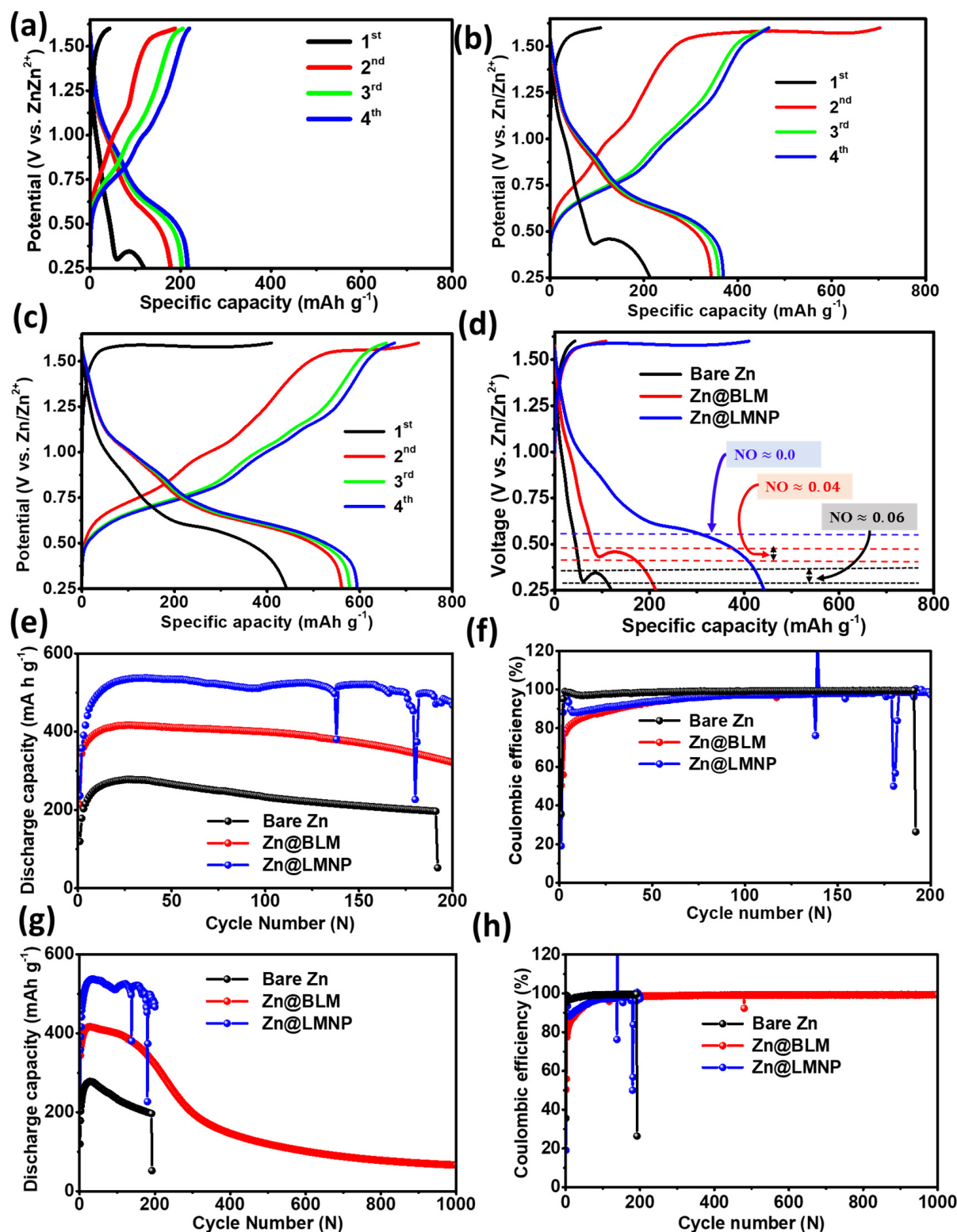


Figure 6. Potential profiles of (a) bare Zn, (b) Zn@BLM, and (c) Zn@LMNP electrodes coupled with $\text{V}_2\text{O}_5@\text{C}$ in 2 M ZnSO_4 and (d) corresponding nucleation overpotential (NO) in the initial discharge process (anodic reaction). Short-term (e) discharge capacity and (f) coulombic efficiency; long-term (g) cyclability and (h) coulombic efficiency of full cells coupled with $\text{V}_2\text{O}_5@\text{C}$ cathode and different anodes. Electrochemical characterizations were conducted in the potential range of 0.25–1.6 V (vs. Zn/Zn^{2+}) at a galvanostatic charge discharge testing rate of 1 A g^{-1} . The capacities were analyzed based on the active mass of the positive electrode.

4. Conclusions

In this study, a room-temperature EGaIn bulk liquid-metal and liquid-metal nanoparticle coating strategy for preventing dendrite formation on Zn electrodes for aqueous rechargeable Zn-ion batteries was proposed. Three different anodes were prepared: bare Zn (control), bulk liquid-metal-coated (Zn@BLM), and liquid-metal nanoparticle-coated (Zn@LMNP) anodes. Liquid metal nanoparticles were prepared using a simple and scalable probe ultrasonication method. Thereafter, symmetric cells and full cells with Zn@BLM and Zn@LMNP electrodes were investigated and compared with cells employing the bare Zn electrode. From symmetric cell studies, it was found that the room-temperature liquid-metal coating could enhance the cyclability and reduce the initial nucleation barrier by an order of magnitude. For instance, at an areal capacity of 0.5 mAh cm^{-2} and a current density of 0.5 mA cm^{-2} , the Zn@BLM || Zn@BLM symmetric cell operated stably for more than 500 h, whereas the bare Zn || Zn symmetric cell failed after ~ 18 h owing to dendrite formation. The Zn@BLM || Zn@BLM symmetric cell also showed the lowest polarization voltage and voltage hysteresis compared to the other symmetric cells under the same experimental conditions. In the full-cell studies, the highest capacity was delivered by the cell with the Zn@LMNP anode; however, this cell was only stable for approximately 200 galvanostatic charge–discharge cycles. In contrast, the cell with the Zn@BLM anode exhibited long cyclability, with a gradual decrease in capacity. Generally, compared to the control, the cells with the bulk liquid-metal and liquid-metal nanoparticle-coated electrodes exhibited much better electrochemical performance, both in symmetric and full cell systems. It can be concluded that liquid-metal coating, especially the liquid-metal nanoparticle coating strategy, is an attractive concept for further investigations.

Supplementary Materials: The following supporting information can be downloaded at: <https://www.mdpi.com/article/10.3390/batteries8110208/s1>, Figure S1: Coulombic efficiencies of the symmetric cells.

Author Contributions: Conceptualization, Methodology, investigation, formal analysis, Writing-original draft preparation, W.G.K.; Methodology, resources, H.Y.; data curation, investigation, S.P.; Conceptualization, Validation, supervision, J.H.; Conceptualization, writing-review and editing, Funding acquisition, supervision, project administration, I.T.K. All authors have read and agreed to the published version of the manuscript.

Funding: This work was supported by the Korea Institute for Advancement of Technology (KIAT) grant funded by the Korea Government (MOTIE) (No.P0012451, No.P0012453, The Competency Development Program for Industry Specialist).

Data Availability Statement: Not applicable.

Conflicts of Interest: The authors declare no conflict of interest.

References

- Chen, D.; Lu, M.; Cai, D.; Yang, H.; Han, W. Recent advances in energy storage mechanism of aqueous zinc-ion batteries. *J. Energy Chem.* **2021**, *54*, 712–726. [[CrossRef](#)]
- Zhang, Y.; Chen, A.; Sun, J. Promise and challenge of vanadium-based cathodes for aqueous zinc-ion batteries. *J. Energy Chem.* **2021**, *54*, 655–667. [[CrossRef](#)]
- Wang, A.; Zhou, W.; Huang, A.; Chen, M.; Tian, Q.; Chen, J. Developing improved electrolytes for aqueous zinc-ion batteries to achieve excellent cyclability and antifreezing ability. *J. Colloid Interface Sci.* **2021**, *586*, 362–370. [[CrossRef](#)] [[PubMed](#)]
- Zhang, N.; Chen, X.; Yu, M.; Niu, Z.; Cheng, F.; Chen, J. Materials chemistry for rechargeable zinc-ion batteries. *Chem. Soc. Rev.* **2020**, *49*, 4203–4219. [[CrossRef](#)] [[PubMed](#)]
- Konarov, A.; Voronina, N.; Jo, J.H.; Bakenov, Z.; Sun, Y.-K.; Myung, S.-T. Present and Future Perspective on Electrode Materials for Rechargeable Zinc-Ion Batteries. *ACS Energy Lett.* **2018**, *3*, 2620–2640. [[CrossRef](#)]
- Kwon, K.Y.; Jo, T.H.; Kim, J.S.; Hasan, F.; Yoo, H.D. A Chronocoulometric Method to Measure the Corrosion Rate on Zinc Metal Electrodes. *ACS Appl. Mater. Interfaces* **2020**, *12*, 42612–42621. [[CrossRef](#)]
- Zhao, Z.; Zhao, J.; Hu, Z.; Li, J.; Li, J.; Zhang, Y.; Wang, C.; Cui, G. Long-life and deeply rechargeable aqueous Zn anodes enabled by a multifunctional brightener-inspired interphase. *Energy Environ. Sci.* **2019**, *12*, 1938–1949. [[CrossRef](#)]

8. Liu, S.; Chen, X.; Zhang, Q.; Zhou, J.; Cai, Z.; Pan, A. Fabrication of an Inexpensive Hydrophilic Bridge on a Carbon Substrate and Loading Vanadium Sulfides for Flexible Aqueous Zinc-Ion Batteries. *ACS Appl. Mater. Interfaces* **2019**, *11*, 36676–36684. [[CrossRef](#)]
9. Cheng, Y.; Luo, L.; Zhong, L.; Chen, J.; Li, B.; Wang, W.; Mao, S.X.; Wang, C.; Sprenkle, V.L.; Li, G.; et al. Highly Reversible Zinc-Ion Intercalation into Chevrel Phase Mo₆S₈ Nanocubes and Applications for Advanced Zinc-Ion Batteries. *ACS Appl. Mater. Interfaces* **2016**, *8*, 13673–13677. [[CrossRef](#)]
10. Huang, S.; Zhu, J.; Tian, J.; Niu, Z. Recent Progress in the Electrolytes of Aqueous Zinc-Ion Batteries. *Chemistry* **2019**, *25*, 14480–14494. [[CrossRef](#)]
11. Zhang, T.; Tang, Y.; Guo, S.; Cao, X.; Pan, A.; Fang, G.; Zhou, J.; Liang, S. Fundamentals and perspectives in developing zinc-ion battery electrolytes: A comprehensive review. *Energy Environ. Sci.* **2020**, *13*, 4625–4665. [[CrossRef](#)]
12. Jia, H.; Wang, Z.; Tawiah, B.; Wang, Y.; Chan, C.-Y.; Fei, B.; Pan, F. Recent advances in zinc anodes for high-performance aqueous Zn-ion batteries. *Nano Energy* **2020**, *70*, 104523. [[CrossRef](#)]
13. Ghosh, M.; Vijayakumar, V.; Kurungot, S. Dendrite Growth Suppression by Zn²⁺-Integrated Nafion Ionomer Membranes: Beyond Porous Separators toward Aqueous Zn/V₂O₅ Batteries with Extended Cycle Life. *Energy Technol.* **2019**, *7*, 1900442. [[CrossRef](#)]
14. Oberholzer, P.; Tervoort, E.; Bouzid, A.; Pasquarello, A.; Kundu, D. Oxide versus Nonoxide Cathode Materials for Aqueous Zn Batteries: An Insight into the Charge Storage Mechanism and Consequences Thereof. *ACS Appl. Mater. Interfaces* **2019**, *11*, 674–682. [[CrossRef](#)] [[PubMed](#)]
15. Yu, Y.; Xu, W.; Liu, X.; Lu, X. Challenges and Strategies for Constructing Highly Reversible Zinc Anodes in Aqueous Zinc-Ion Batteries: Recent Progress and Future Perspectives. *Adv. Sustain. Syst.* **2020**, *4*, 2000082. [[CrossRef](#)]
16. Li, C.; Xie, X.; Liang, S.; Zhou, J. Issues and Future Perspective on Zinc Metal Anode for Rechargeable Aqueous Zinc-ion Batteries. *Energy Environ. Mater.* **2020**, *3*, 146–159. [[CrossRef](#)]
17. Zeng, X.; Hao, J.; Wang, Z.; Mao, J.; Guo, Z. Recent progress and perspectives on aqueous Zn-based rechargeable batteries with mild aqueous electrolytes. *Energy Storage Mater.* **2019**, *20*, 410–437. [[CrossRef](#)]
18. Bayaguud, A.; Fu, Y.; Zhu, C. Interfacial parasitic reactions of zinc anodes in zinc ion batteries: Underestimated corrosion and hydrogen evolution reactions and their suppression strategies. *J. Energy Chem.* **2022**, *64*, 246–262. [[CrossRef](#)]
19. Yang, G.; Li, Q.; Ma, K.; Hong, C.; Wang, C. The degradation mechanism of vanadium oxide-based aqueous zinc-ion batteries. *J. Mater. Chem. A* **2020**, *8*, 8084–8095. [[CrossRef](#)]
20. Cao, H.; Huang, X.; Liu, Y.; Hu, Q.; Zheng, Q.; Huo, Y.; Xie, F.; Zhao, J.; Lin, D. An efficient electrolyte additive of tetramethylammonium sulfate hydrate for Dendritic-Free zinc anode for aqueous Zinc-ion batteries. *J. Colloid Interface Sci.* **2022**, *627*, 367–374. [[CrossRef](#)]
21. Qiu, B.; Xie, L.; Zhang, G.; Cheng, K.; Lin, Z.; Liu, W.; He, C.; Zhang, P.; Mi, H. Toward reversible wide-temperature Zn storage by regulating the electrolyte solvation structure via trimethyl phosphate. *Chem. Eng. J.* **2022**, *449*, 137843. [[CrossRef](#)]
22. Hieu, L.T.; So, S.; Kim, I.T.; Hur, J. Zn anode with flexible β-PVDF coating for aqueous Zn-ion batteries with long cycle life. *Chem. Eng. J.* **2021**, *411*, 128584. [[CrossRef](#)]
23. Zhao, K.; Wang, C.; Yu, Y.; Yan, M.; Wei, Q.; He, P.; Dong, Y.; Zhang, Z.; Wang, X.; Mai, L. Ultrathin Surface Coating Enables Stabilized Zinc Metal Anode. *Adv. Mater. Interfaces* **2018**, *5*, 1800848. [[CrossRef](#)]
24. Guo, J.; Ming, J.; Lei, Y.; Zhang, W.; Xia, C.; Cui, Y.; Alshareef, H.N. Artificial Solid Electrolyte Interphase for Suppressing Surface Reactions and Cathode Dissolution in Aqueous Zinc Ion Batteries. *ACS Energy Lett.* **2019**, *4*, 2776–2781. [[CrossRef](#)]
25. Zhao, R.; Yang, Y.; Liu, G.; Zhu, R.; Huang, J.; Chen, Z.; Gao, Z.; Chen, X.; Qie, L. Redirected Zn Electrodeposition by an Anti-Corrosion Elastic Constraint for Highly Reversible Zn Anodes. *Adv. Funct. Mater.* **2020**, *31*, 2001867. [[CrossRef](#)]
26. Li, W.; Wang, K.; Zhou, M.; Zhan, H.; Cheng, S.; Jiang, K. Advanced Low-Cost, High-Voltage, Long-Life Aqueous Hybrid Sodium/Zinc Batteries Enabled by a Dendrite-Free Zinc Anode and Concentrated Electrolyte. *ACS Appl. Mater. Interfaces* **2018**, *10*, 22059–22066. [[CrossRef](#)]
27. Kang, Z.; Wu, C.; Dong, L.; Liu, W.; Mou, J.; Zhang, J.; Chang, Z.; Jiang, B.; Wang, G.; Kang, F.; et al. 3D Porous Copper Skeleton Supported Zinc Anode toward High Capacity and Long Cycle Life Zinc Ion Batteries. *ACS Sustain. Chem. Eng.* **2019**, *7*, 3364–3371. [[CrossRef](#)]
28. Li, C.; Shi, X.; Liang, S.; Ma, X.; Han, M.; Wu, X.; Zhou, J. Spatially homogeneous copper foam as surface dendrite-free host for zinc metal anode. *Chem. Eng. J.* **2020**, *379*, 122248. [[CrossRef](#)]
29. Ke, X.; Liang, Y.; Ou, L.; Liu, H.; Chen, Y.; Wu, W.; Cheng, Y.; Guo, Z.; Lai, Y.; Liu, P.; et al. Surface engineering of commercial Ni foams for stable Li metal anodes. *Energy Storage Mater.* **2019**, *23*, 547–555. [[CrossRef](#)]
30. Yang, C.; Yao, Y.; He, S.; Xie, H.; Hitz, E.; Hu, L. Ultrafine Silver Nanoparticles for Seeded Lithium Deposition toward Stable Lithium Metal Anode. *Adv. Mater.* **2017**, *29*, 1702714. [[CrossRef](#)]
31. Liang, Y.; Chen, Y.; Ke, X.; Zhang, Z.; Wu, W.; Lin, G.; Zhou, Z.; Shi, Z. Coupling of triporosity and strong Au–Li interaction to enable dendrite-free lithium plating/stripping for long-life lithium metal anodes. *J. Mater. Chem. A* **2020**, *8*, 18094–18105. [[CrossRef](#)]
32. Wu, Y.; Huang, L.; Huang, X.; Guo, X.; Liu, D.; Zheng, D.; Zhang, X.; Ren, R.; Qu, D.; Chen, J. A room-temperature liquid metal-based self-healing anode for lithium-ion batteries with an ultra-long cycle life. *Energy Environ. Sci.* **2017**, *10*, 1854–1861. [[CrossRef](#)]
33. Wei, C.; Fei, H.; An, Y.; Tao, Y.; Feng, J.; Qian, Y. Uniform Li deposition by regulating the initial nucleation barrier via a simple liquid-metal coating for a dendrite-free Li–metal anode. *J. Mater. Chem. A* **2019**, *7*, 18861–18870. [[CrossRef](#)]

34. Guo, X.; Zhang, L.; Ding, Y.; Goodenough, J.B.; Yu, G. Room-temperature liquid metal and alloy systems for energy storage applications. *Energy Environ. Sci.* **2019**, *12*, 2605–2619. [[CrossRef](#)]
35. Tang, S.-Y.; Tabor, C.; Kalantar-Zadeh, K.; Dickey, M.D. Gallium Liquid Metal: The Devil’s Elixir. *Annu. Rev. Mater. Res.* **2021**, *51*, 381–408. [[CrossRef](#)]
36. Wang, X.; Guo, R.; Liu, J. Liquid Metal Based Soft Robotics: Materials, Designs, and Applications. *Adv. Mater. Technol.* **2018**, *4*, 1800549. [[CrossRef](#)]
37. Cochran, C.N.; Foster, L.M. Vapor Pressure of Gallium, Stability of Gallium Suboxide Vapor, and Equilibria of Some Reactions Producing Gallium Suboxide Vapor. *J. Electrochem. Soc.* **1962**, *109*, 144. [[CrossRef](#)]
38. Kidanu, W.G.; Hur, J.; Kim, I.T. Gallium-Indium-Tin Eutectic as a Self-Healing Room-Temperature Liquid Metal Anode for High-Capacity Lithium-Ion Batteries. *Materials* **2021**, *15*, 168. [[CrossRef](#)]
39. Khamsanga, S.; Uyama, H.; Nuanwat, W.; Pattananuwat, P. Polypyrrole/reduced graphene oxide composites coated zinc anode with dendrite suppression feature for boosting performances of zinc ion battery. *Sci. Rep.* **2022**, *12*, 8689. [[CrossRef](#)]
40. Song, B.; Tang, M.; Hu, E.; Borkiewicz, O.J.; Wiaderek, K.M.; Zhang, Y.; Phillip, N.D.; Liu, X.; Shadike, Z.; Li, C.; et al. Understanding the Low-Voltage Hysteresis of Anionic Redox in $\text{Na}_2\text{Mn}_3\text{O}_7$. *Chem. Mater.* **2019**, *31*, 3756–3765. [[CrossRef](#)]
41. Zheng, X.; Fu, H.; Hu, C.; Xu, H.; Huang, Y.; Wen, J.; Sun, H.; Luo, W.; Huang, Y. Toward a Stable Sodium Metal Anode in Carbonate Electrolyte: A Compact, Inorganic Alloy Interface. *J. Phys. Chem. Lett.* **2019**, *10*, 707–714. [[CrossRef](#)]
42. Zhao, Y.; Goncharova, L.V.; Zhang, Q.; Kaghazchi, P.; Sun, Q.; Lushington, A.; Wang, B.; Li, R.; Sun, X. Inorganic-Organic Coating via Molecular Layer Deposition Enables Long Life Sodium Metal Anode. *Nano Lett.* **2017**, *17*, 5653–5659. [[CrossRef](#)]
43. Liao, K.; Wu, S.; Mu, X.; Lu, Q.; Han, M.; He, P.; Shao, Z.; Zhou, H. Developing a “Water-Defendable” and “Dendrite-Free” Lithium-Metal Anode Using a Simple and Promising GeCl_4 Pretreatment Method. *Adv. Mater.* **2018**, *30*, e1705711. [[CrossRef](#)]
44. Pang, Q.; Liang, X.; Shyamsunder, A.; Nazar, L.F. An In Vivo Formed Solid Electrolyte Surface Layer Enables Stable Plating of Li Metal. *Joule* **2017**, *1*, 871–886. [[CrossRef](#)]
45. Zhao, Y.; Yang, X.; Kuo, L.Y.; Kaghazchi, P.; Sun, Q.; Liang, J.; Wang, B.; Lushington, A.; Li, R.; Zhang, H.; et al. High Capacity, Dendrite-Free Growth, and Minimum Volume Change Na Metal Anode. *Small* **2018**, *14*, e1703717. [[CrossRef](#)]
46. Baumgartner, J.; Dey, A.; Bomans, P.H.; Le Coadou, C.; Fratzl, P.; Sommerdijk, N.A.; Faire, D. Nucleation and growth of magnetite from solution. *Nat. Mater.* **2013**, *12*, 310–314. [[CrossRef](#)]
47. Yue, X.-Y.; Wang, W.-W.; Wang, Q.-C.; Meng, J.-K.; Zhang, Z.-Q.; Wu, X.-J.; Yang, X.-Q.; Zhou, Y.-N. CoO nanofiber decorated nickel foams as lithium dendrite suppressing host skeletons for high energy lithium metal batteries. *Energy Storage Mater.* **2018**, *14*, 335–344. [[CrossRef](#)]
48. Yan, K.; Lu, Z.; Lee, H.-W.; Xiong, F.; Hsu, P.-C.; Li, Y.; Zhao, J.; Chu, S.; Cui, Y. Selective deposition and stable encapsulation of lithium through heterogeneous seeded growth. *Nat. Energy* **2016**, *1*, 16010. [[CrossRef](#)]
49. Guan, X.; Wang, A.; Liu, S.; Li, G.; Liang, F.; Yang, Y.W.; Liu, X.; Luo, J. Controlling Nucleation in Lithium Metal Anodes. *Small* **2018**, *14*, e1801423. [[CrossRef](#)]
50. Liu, L.; Yin, Y.X.; Li, J.Y.; Wang, S.H.; Guo, Y.G.; Wan, L.J. Uniform Lithium Nucleation/Growth Induced by Lightweight Nitrogen-Doped Graphitic Carbon Foams for High-Performance Lithium Metal Anodes. *Adv. Mater.* **2018**, *30*, 1706216. [[CrossRef](#)]
51. Wu, W.; Wu, W.; Qiu, X.; Wang, S. Low-temperature reversible capacity loss and aging mechanism in lithium-ion batteries for different discharge profiles. *Int. J. Energy Res.* **2018**, *43*, 243–253. [[CrossRef](#)]
52. Jiang, Y.; Jiang, Z.-J.; Yang, L.; Cheng, S.; Liu, M. A high-performance anode for lithium ion batteries: Fe_3O_4 microspheres encapsulated in hollow graphene shells. *J. Mater. Chem. A* **2015**, *3*, 11847–11856. [[CrossRef](#)]
53. Wang, D.; Zhang, W.; Zheng, W.; Cui, X.; Rojo, T.; Zhang, Q. Towards High-Safe Lithium Metal Anodes: Suppressing Lithium Dendrites via Tuning Surface Energy. *Adv. Sci.* **2017**, *4*, 1600168. [[CrossRef](#)]
54. Lin, Y.; Genzer, J.; Dickey, M.D. Attributes, Fabrication, and Applications of Gallium-Based Liquid Metal Particles. *Adv. Sci.* **2020**, *7*, 2000192. [[CrossRef](#)]